J Mater Sci: Mater Electron (2026) 37:316

Triacetoxyvinylsilane-based polymer intercalated-graphene for enhanced 3D Ni foam electrodes in energy storage applications

P. Balcı[1], S. R. Tokgöz[2], A. Kara[1], and A. Peksöz[2,*]

[1] *Chemistry Department, Faculty of Arts and Sciences, Uludağ University, Görükle Campus, 16059 Bursa, Turkey*
[2] *Physics Department, Faculty of Arts and Sciences, Uludağ University, Görükle Campus, 16059 Bursa, Turkey*

Received: 22 August 2025
Accepted: 18 January 2026

© The Author(s), 2026

ABSTRACT

This study demonstrates the exceptional supercapacitive performance of a novel P(EGDMA-TAVS)–graphene composite on nickel foam (NF) substrate. The three-dimensional porous architecture, combining the high conductivity of graphene with the robust polymeric framework of poly(ethylene glycol dimethacrylate-trimethylolpropane allyl ether vinyl sulfonate) [P(EGDMA-TAVS)], enables outstanding electrochemical properties. The p(EGDMA-TAVS)–graphene/NF electrode demonstrates specific capacitances of 963.9, 817.2, 746.1, 716.4, 650.6, and 603.5 F g^{-1} when tested at scan rates of 10, 20, 30, 50, and 70 mV s^{-1}, respectively. The enhanced interfacial adhesion provided by p(EGDMA-TAVS), together with graphene's efficient electron-transport network on the nickel foam current collector, yields an energy density of 40.3 Wh kg^{-1} at a power density of 4773.6 W kg^{-1} in 3 M KOH. The p(EGDMA-TAVS)–graphene/NF electrode preserves 95.6% of its starting capacitance over 2500 cycles at 6 A g^{-1}. These results position the P(EGDMA-TAVS)-graphene/NF electrode as a promising candidate for high-performance energy storage applications.

1 Introduction

The increasing global demand for efficient and reliable energy storage devices has spurred significant interest in supercapacitors, which play a crucial role in applications ranging from portable electronics to electric vehicles [1, 2]. Supercapacitors are distinguished by their high power density, rapid charge/discharge capabilities, and long cycle life compared to conventional batteries. Despite these advantages, their relatively low energy density remains a primary limitation for widespread adoption [3, 4]. Consequently, considerable research has focused on developing advanced electrode materials and architectures that synergistically combine electric double-layer capacitance (EDLC) and pseudocapacitance to overcome this limitation [5, 6]. Graphene, a two-dimensional carbon allotrope, has emerged as an ideal candidate for high-performance supercapacitor electrodes due to its exceptional electrical conductivity (~10^3 S/cm), large theoretical surface area (~ 2630 m^2/g), and excellent mechanical strength [2, 3]. However, practical application of graphene often

Address correspondence to E-mail: peksoz@uludag.edu.tr

https://doi.org/10.1007/s10854-026-16724-z
Published online: 05 February 2026

encounters challenges such as aggregation, poor dispersion, and limited interaction with polymeric binders [4, 6]. To mitigate these issues, three-dimensional conductive substrates, such as nickel foam (NF), have been employed. The highly porous NF framework enhances electron transport, provides mechanical support, and increases the effective surface area for active material deposition, ultimately improving electrode performance [1, 5].

Recent studies have demonstrated the benefits of integrating graphene with polymeric matrices for enhanced supercapacitor performance. For instance, Xu et al. [7] developed a graphene oxide/PEDOT-based composite hydrogel, achieving a high specific capacitance of 441 F g^{-1} and remarkable long-term cycling stability (95.2% retention after 10000 cycles). Tan et al. [8] synthesized graphene/polyaniline composites on NF substrates, showing substantial enhancements in capacitance and rate capability due to the synergistic contributions of graphene's conductive network and polyaniline's pseudocapacitive properties. Similarly, Zheng et al. [9] fabricated MnO_2/graphene/NF composites, which exhibited high energy density and excellent electron/ion transport pathways. Collectively, these studies highlight the importance of designing hybrid materials that combine conductive carbon nanostructures with functional polymers to achieve superior electrochemical performance.

Building on these insights, the present study examines the electrochemical behavior of a P(EGDMA-TAVS)–graphene composite electrode supported on a nickel foam substrate. The design leverages graphene's high electrical conductivity and large surface area, while the P(EGDMA-TAVS) network enhances mechanical robustness and promotes strong interfacial adhesion to the nickel foam. The three-dimensional porous structure of NF provides rapid electrolyte access and a continuous conductive network, maximizing the utilization of the active material. Electrochemical performance is evaluated using cyclic voltammetry (CV) and galvanostatic charge–discharge (GCD) measurements, focusing on specific capacitance, energy density, rate capability, and cycling stability. Recent breakthroughs in electrode engineering emphasize the critical role of controlled interfacial design in advancing supercapacitor performance. While conventional slurry-cast electrodes often suffer from inhomogeneous binder distribution and inefficient ion pathways, in situ polymerization techniques have emerged as a promising alternative to construct integrated electrode architectures. This study introduces a precisely controlled surface polymerization strategy to fabricate P(EGDMA–TAVS)–graphene/NF electrodes, where the polymer phase is molecularly anchored to the graphene/NF scaffold, addressing long-standing challenges in materials synthesis and charge storage mechanisms.

2 Experimental

2.1 Materials

Triacetoxyvinylsilane (TAVS), ethylene glycol dimethacrylate (EGDMA), 2,2′-Azobis(2-methylpropionitrile (AIBN), and potassium hydroxide (KOH) were purchased from Sigma-Aldrich Company (UK). The chemical compounds used in this study have a purity exceeding 98% and were employed as received without additional purification. Nickel foam (NF) was sourced commercially from Nanografi Co. Inc., Turkey. A nickel foam substrate with a surface area of 1 cm^2 and a sheet resistance of 10 Ω/sq served as the working electrode. Before electrodeposition, the nickel foam was thoroughly cleaned via ultrasonication in a sequence of deionized water, HCl, acetone, and isopropanol (C_3H_8O) for 75 min. After cleaning, the substrate was dried under a stream of nitrogen gas. The graphene used in this study (Nanografi brand) exhibits a sheet resistivity of 1155 Ω/sq, an electrical conductivity exceeding 800 S/m, a volume resistivity of 0.11 Ω·cm, and a pore size distribution ranging from 2 to 100 nm.

2.2 *Preparation of p(EGDMA-TAVS)/NF and p(EGDMA-TAVS) –graphene/NF electrodes*

The fabrication of p(EGDMA-TAVS)–graphene/NF electrodes were prepared through a sequential fabrication procedure. First, a homogeneous solution was prepared by mixing 3 mL of EGDMA, 5 mL of TAVS, 0.1 g of AIBN, and graphene in a reaction vessel. The mixture was magnetically stirred at 25 °C for 15 min to ensure complete dissolution, followed by the addition of 0.2 g of graphene with an additional 3 min of stirring. Next, the solution was drop-cast onto nickel foam substrates, ensuring uniform coating. Polymerization was initiated by immersing the coated foam in a 70 °C water bath for 30 min. Finally, the sample

underwent a drying process, where it was first maintained in the water bath and then transferred to an oven at 70 °C for 6 h. To promote uniform drying and prevent aggregation, the electrode was positioned at a 20° inclination within the drying chamber. The schematic representation of the molecular structure of p(EGDMA-TAVS)–graphene is shown in Fig. 1. The synthesis of p(EGDMA-TAVS)/NF follows an identical procedure, except that no graphene is incorporated into the solution. The graphene doping in the p(EGDMA-TAVS)–graphene electrode is approximately 3% by weight.

2.3 Structural characterizations and electrochemical measurements

The chemical bonding characteristics of p(EGDMA-TAVS) and its graphene-modified counterpart were investigated using FTIR spectroscopy (Shimadzu IRTracer-100). Raman spectra were recorded using

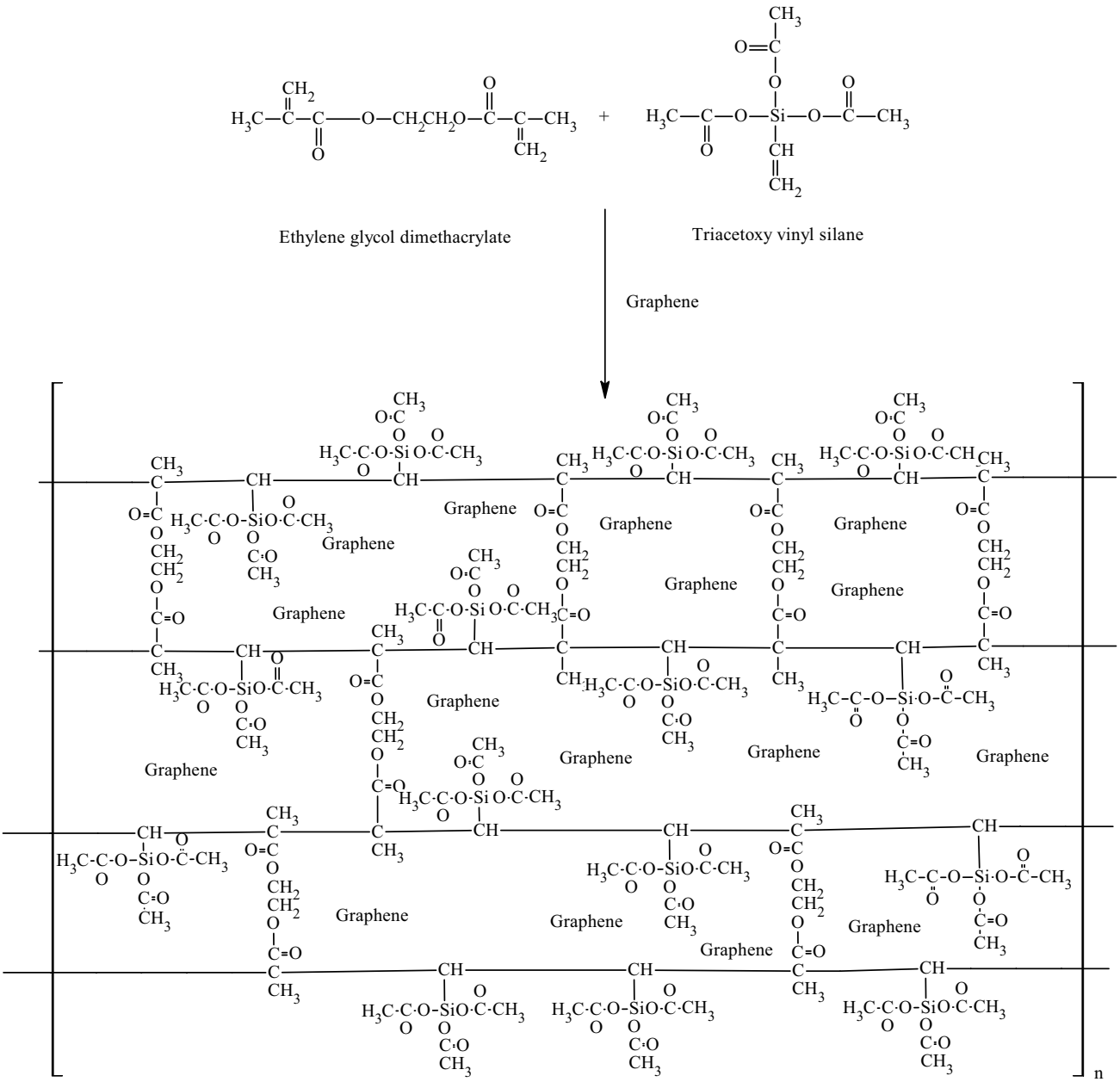


Fig. 1 Schematic representation of the p(EGDMA-TAVS)–GRAPHENE synthesis

a Renishaw Raman Microscope. Molecular binding interactions were verified by X-ray photoelectron spectroscopy (XPS) using a SPECS Surface Nano Analysis system. High-resolution morphological examination was performed using field-emission SEM (FEI Quanta 200 FEG). TGA was conducted from room temperature to 900 °C at 10 °C min^{-1} under nitrogen using a Shimadzu DTG-60H. The electrochemical characterization was conducted using a comprehensive suite of analytical techniques. Impedance spectroscopy measurements were performed across a broad frequency spectrum (0.01 Hz to 300 kHz) with a 5 mV AC amplitude, followed by equivalent circuit analysis using Gamry's Echem software to model the electrode–electrolyte interface. The redox characteristics were examined through cyclic voltammetry, while the charge storage capacity and cycling stability were evaluated using galvanostatic charge–discharge tests. All electrochemical assessments were carried out in a three-electrode configuration utilizing 3 M potassium hydroxide as the electrolyte medium, ensuring consistent experimental conditions for comparative analysis of the electrode materials' performance characteristics.

3 Results and discussion

3.1 Surface profiles

Figure 2 compares the surface morphologies of (a) pristine NF, (b) p(EGDMA-TAVS)/NF, and (c) p(EGDMA-TAVS)–graphene/NF. The polymer fully infiltrates NF's 3D pores (Fig. 2b), with submicron particles (200–500 nm) visible at higher magnification. The graphene hybrid (Fig. 2c) develops microcracked plates with nanoscale surface features (50 nm–1 µm), creating hierarchical porosity. The addition of graphene clearly creates a highly rough

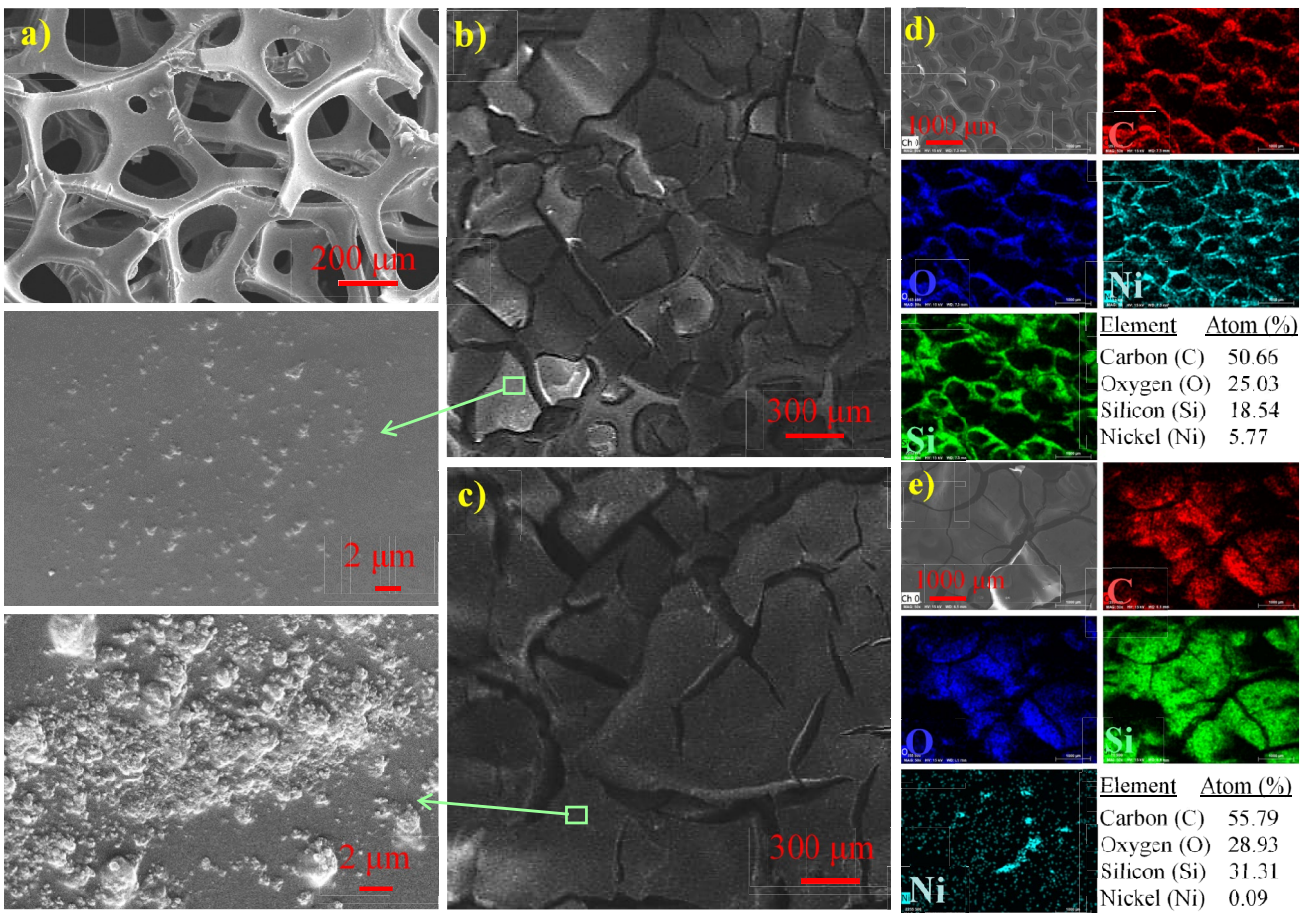


Fig. 2 SEM image of **a** nickel foam, **b** p(EGDMA-TAVS)/NF, and **c** p(EGDMA-TAVS)–graphene/NF, **d** EDS mapping of p(EGDMA-TAVS)/NF, **e** EDS mapping of p(EGDMA-TAVS)–graphene/NF

surface morphology, which implies increased surface area for ion interaction. The SEM surface images demonstrate excellent material adhesion through surface polymerization, suggesting significant advantages for charge–discharge cycle stability. Furthermore, the surface polymerization method enables embedding of the material into NF's 3D structure with chemical bonding, allowing high loading of active material on the electrode. Figure 2d, e displays the EDS mappings of the p(EGDMA-TAVS) and p(EGDMA-TAVS)–GRAPHENE electrodes, respectively. The maps indicate that Carbon (C), Oxygen (O), Silicon (Si), and Nickel (Ni) are evenly distributed across the surfaces of both electrodes. For the p(EGDMA-TAVS) electrode, the percentages of C, O, Si, and Ni are 50.66, 25.03, 18.54, and 5.77%, respectively, whereas for the p(EGDMA-TAVS)–GRAPHENE electrode, they are 55.79, 28.93%, 31.31, and 0.09%, respectively. Additionally, the noticeable decrease in Ni content after graphene incorporation suggests a more complete coverage of the substrate surface, likely due to the increased film density or improved surface uniformity. The higher Si percentage in the graphene-doped electrode may also indicate enhanced integration of the silane-based structure within the electrode layer. These observations support the improved structural organization achieved after graphene addition.

3.2 FTIR, Raman and XPS studies

The chemical composition and molecular interactions in p(EGDMA-TAVS) and its graphene composite were characterized by FTIR spectroscopy (Fig. 3a). The strong absorption band at 1727.5 cm^{-1} corresponds to the stretching vibrations of ester carbonyl (C=O) groups in the EGDMA monomer, confirming the successful incorporation of the diacrylate monomer into the polymer matrix and the occurrence of polymerization. The absorption around 2958.2 cm^{-1} is attributed to the aliphatic C–H stretching vibrations of $–CH_2$ and $–CH_3$ groups present in both EGDMA and TAVS units [10]. The band at 1273.9 cm^{-1} is attributed to C–O–C stretching vibrations from ester groups and may also involve Si–C vibrations arising from the silane structure of TAVS [10]. A pronounced band at 1410.1 cm^{-1} emerges upon the addition of graphene, which is assigned to the aromatic C=C skeletal vibrations, indicating the integration of graphene into the polymer matrix and likely π–π interactions with polymer chains [11]. The band at 993.6 cm^{-1} may indicate in-plane C–H bending vibrations arising from vinyl groups or the conjugated π-system of graphene. The absorption at 758.6 cm^{-1} may originate from out-of-plane C–H bending vibrations in aromatic systems or from Si–C bonds attributed to TAVS [10]. Finally, the weak band observed around 538.0 cm^{-1} is most likely

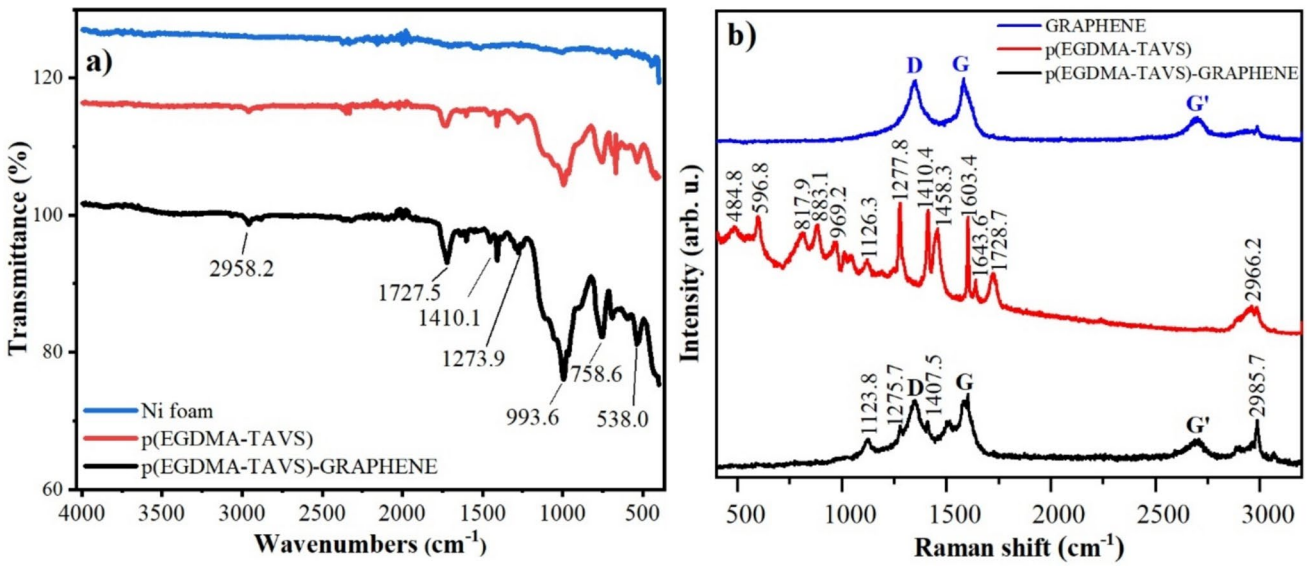


Fig. 3 **a** FTIR spectrum of the pure nickel foam, p(EGDMA-TAVS), and p(EGDMA-TAVS)–graphene, **b** Raman spectrum of the graphene, p(EGDMA-TAVS), and p(EGDMA-TAVS)–graphene

associated with Si–O–Si bending vibrations from TAVS or Ni–O stretching modes potentially arising from the surface of the nickel foam [10]. These findings confirm the successful copolymerization of EGDMA and TAVS and the effective incorporation of graphene into the polymer matrix. Furthermore, the preservation of characteristic vibrational bands of functional groups supports the structural integrity of the material during the synthesis process.

The Raman spectra of p(EGDMA-TAVS), p(EGDMA-TAVS)–GRAPHENE, and pure graphene are shown in Fig. 3b. Pristine graphene exhibits the typical D (1341.9 cm^{-1}), G (1580.7 cm^{-1}), and G′ (2699.2 cm^{-1}) bands (Fig. 3b). The *D* band corresponds to defects and disorder in the sp^2 carbon framework, while the G band represents in-plane vibrations of sp^2-bonded carbon atoms. Additionally, a secondary feature, the 2D (or G′) band at 2699.9 cm^{-1}, arises from a two-phonon second-order process influenced by double-resonance Raman scattering [11]. The G′ band also reflects the stacking order and number of graphene layers. The Raman spectrum of p(EGDMA-TAVS) electrode reveals multiple distinct vibrational features (Fig. 3b). A band observed at 484.8 cm^{-1} can be attributed to Si–O–Si bending vibrations, reflecting the formation of the siloxane network. The peak at 596.8 cm^{-1} likely arises from Si–C stretching or C–C–C skeletal bending [12]. Vibrations around 817.9 cm^{-1} and 883.1 cm^{-1} are associated with vinyl C–H out-of-plane bending, while the feature at 969.2 cm^{-1} corresponds to C=C–H bending. Bands at 1126.3 cm^{-1} and 1217.8 cm^{-1} can be assigned to C–O–C stretching from ethylene glycol units or Si–O–C linkages. Deformation vibrations of CH_2 and CH_3 groups from methacrylate and acetoxy functionalities are observed at 1410.4 cm^{-1} and 1458.3 cm^{-1}. Peaks at 1603.4 cm^{-1} and 1643.6 cm^{-1} indicate C=C stretching from vinyl and methacrylate groups, whereas the strong band at 1728.7 cm^{-1} is characteristic of C=O stretching [10]. Finally, the high-frequency feature at 2966.2 cm^{-1} arises from aliphatic C–H stretching [10]. In the polymer–graphene composite, the spectra show the characteristic D and G bands of graphene along with features of the polymer (Fig. 3b). This indicates successful incorporation of the polymer onto the graphene surface while maintaining the structural features of graphene. The relative intensities and slight shifts in the D and G bands suggest interactions between the polymer chains and the graphene surface, potentially altering the electronic environment of the carbon lattice. Overall, the Raman analysis confirms both the presence of polymer functional groups and the retention of graphene's structural integrity within the composite.

The XPS spectrum of the electrodes (Fig. 4a) shows pronounced signals at 531.2 and 283.1 eV, corresponding to the O 1 s and C 1 s binding energies, respectively. The peaks at 101.0 and 152.1 eV correspond to Si2p and Si2s, respectively (Fig. 4a). The XPS peaks at 976.1 and 999.0 eV are ascribed to O KLL Auger transitions (Fig. 4a). The atomic compositions are 58.4% C, 32.7% O, and 8.9% Si for the p(EGDMA-TAVS)/NF electrode, and 64.0 C, 30.8 O, and 5.2% Si for the p(EGDMA-TAVS)–graphene/NF electrode. The decreased intensity of Si and O peaks after graphene incorporation, coupled with the increased carbon content ($\Delta C = +5.6$ at%), provides clear evidence of successful graphene integration into the composite structure. This is further supported by the relative attenuation of silicon signals (The Si content shows a reduction of 3.7 at%).

High-resolution XPS of the prepared electrodes reveals a chemically complex surface composed of silicon–oxygen networks, oxygenated carbon species derived from the polymer backbone, and a substantial hydrocarbon/sp^2 carbon contribution consistent with the addition of graphene. Deconvolution of the O 1 s, C 1 s, and Si 2p envelopes gives a consistent picture: the oxygen signal is partitioned into a Si–O component and oxygen atoms bound to carbonyl/ester environments; the carbon envelope is dominated by C–C/C=C with progressively more oxygenated components at higher binding energy; and the silicon envelope shows both Si–O and Si–C contributions. These assignments indicate that the TAVS-derived silicon functionality is present in two chemical states (oxidized and carbon-bound), while the EGDMA-derived network supplies ester/carbonyl oxygen and C–O linkages.

The O 1 s spectrum (Fig. 4b) is fitted with three components at 531.9, 530.5, and 528.7 eV, which are assigned to O–Si, O–C=O (ester/carboxylate), and O=C (carbonyl), respectively. The relative presence of an O–Si component confirms the formation of a silicon–oxygen network at the electrode surface, while the O–C=O and O=C peaks are consistent with ester and carbonyl moieties originating from the EGDMA cross-linked polymer. In the C 1 s envelope (Fig. 4c), four components at 286.2, 284.7, 283.4, and 282.2 eV correspond to O–C=O, C=O, C–O, and C–C/C=C. Finally, the Si 2p spectrum (Fig. 4d) shows two peaks at 100.7 and 100.0 eV assigned to Si–O and Si–C, indicating

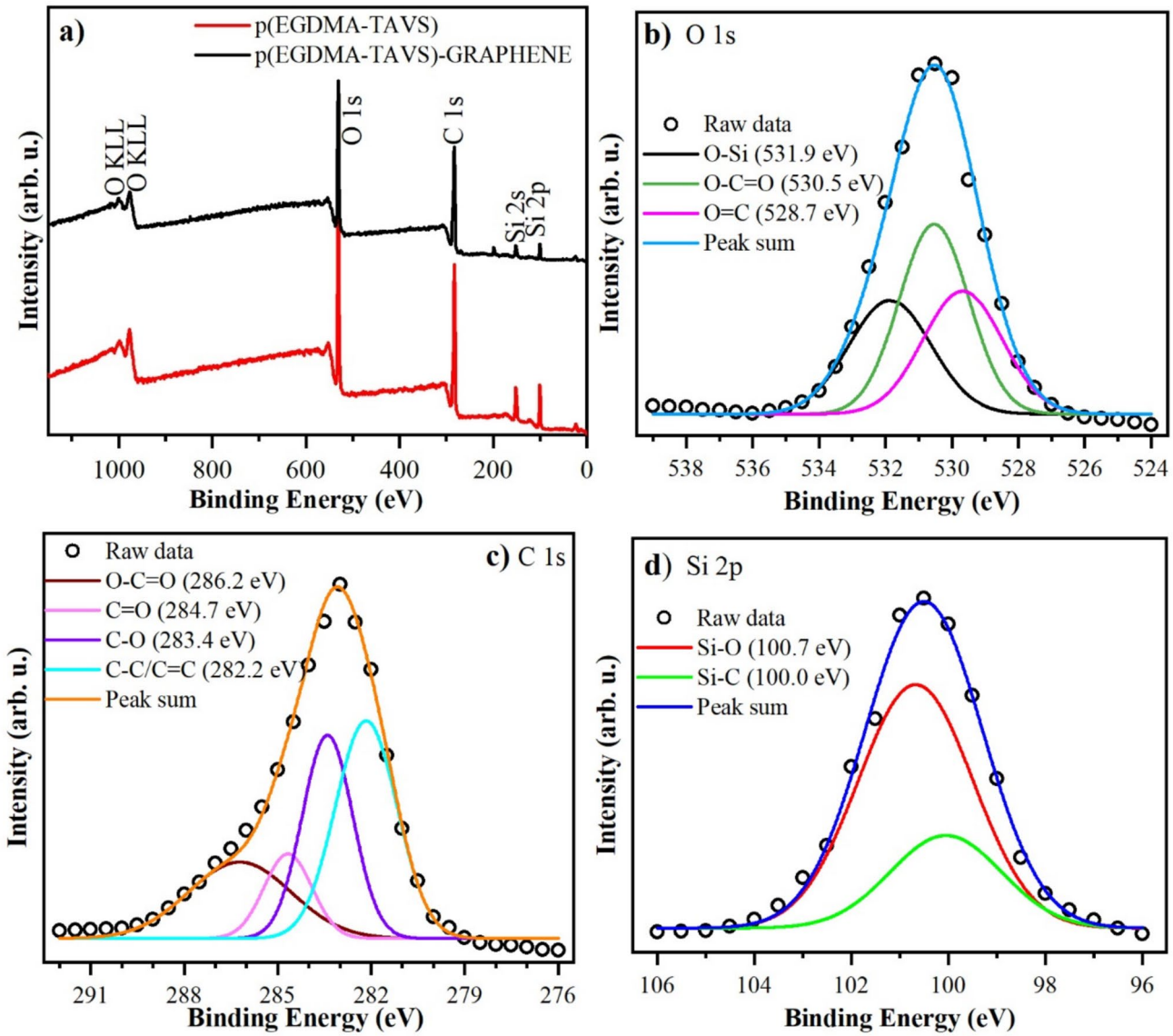


Fig. 4 **a** XPS survey scan of the p(EGDMA-TAVS), and p(EGDMA-TAVS)–graphene, and high-resolution XPS spectrum of **b** O 1 s, **c** C 1 s, and **d** Si 2p

that silicon exists both as part of an oxidic network and as covalently bound silicon–carbon linkages.

3.3 TGA analysis

The p(EGDMA-TAVS)–graphene composite exhibits a multi-stage mass loss during thermogravimetric analysis, ultimately losing approximately 45.5% of its mass by 900 °C (Fig. 5). An initial, minor mass reduction below 150 °C stems from the evolution of physically adsorbed water and residual solvents. A more gradual mass decline follows up to about 290 °C, signaling the scission of less stable ester bonds and initial changes to the cross-linked structure. The most significant degradation step occurs between 290 and 520 °C, which is associated with the primary decomposition of the polymer's backbone (Fig. 5). Above 520 °C, the mass stabilizes, indicating the production of a stable carbon-rich char. The remaining mass at high temperatures highlights the stabilizing contribution of graphene, which supports char formation and mitigates complete thermal degradation of the organic components. Overall, the thermal response suggests a composite architecture in which graphene enhances

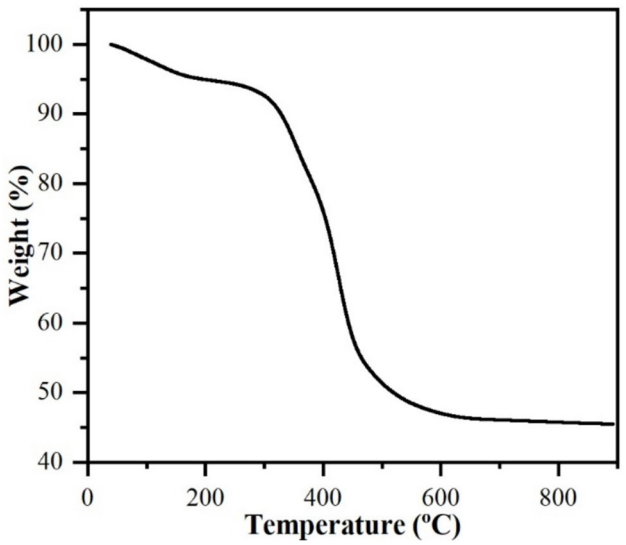


Fig. 5 TGA curve of p(EGDMA-TAVS)–graphene

the high-temperature durability of the polymer–carbon hybrid structure.

3.4 Electrochemical performance

The cyclic voltammetry (CV) and galvanostatic charge–discharge (GCD) tests were carried out to investigate the electrochemical and supercapacitive performance of the p(EGDMA-TAVS)–graphene/NF electrode. All electrochemical measurements were performed in a 3 M KOH aqueous electrolyte using a standard three-electrode configuration, where an Ag/AgCl electrode served as the reference. The CV profiles were recorded within a potential window of − 0.5 to 0.2 V (vs. Ag/AgCl). Figure 6a presents the CV curves of the p(EGDMA-TAVS)–graphene/NF electrode at scan rates ranging from 10 to 100 mV s^{-1}. As shown, the integrated area of the CV curves expands progressively with increasing scan rate, indicating

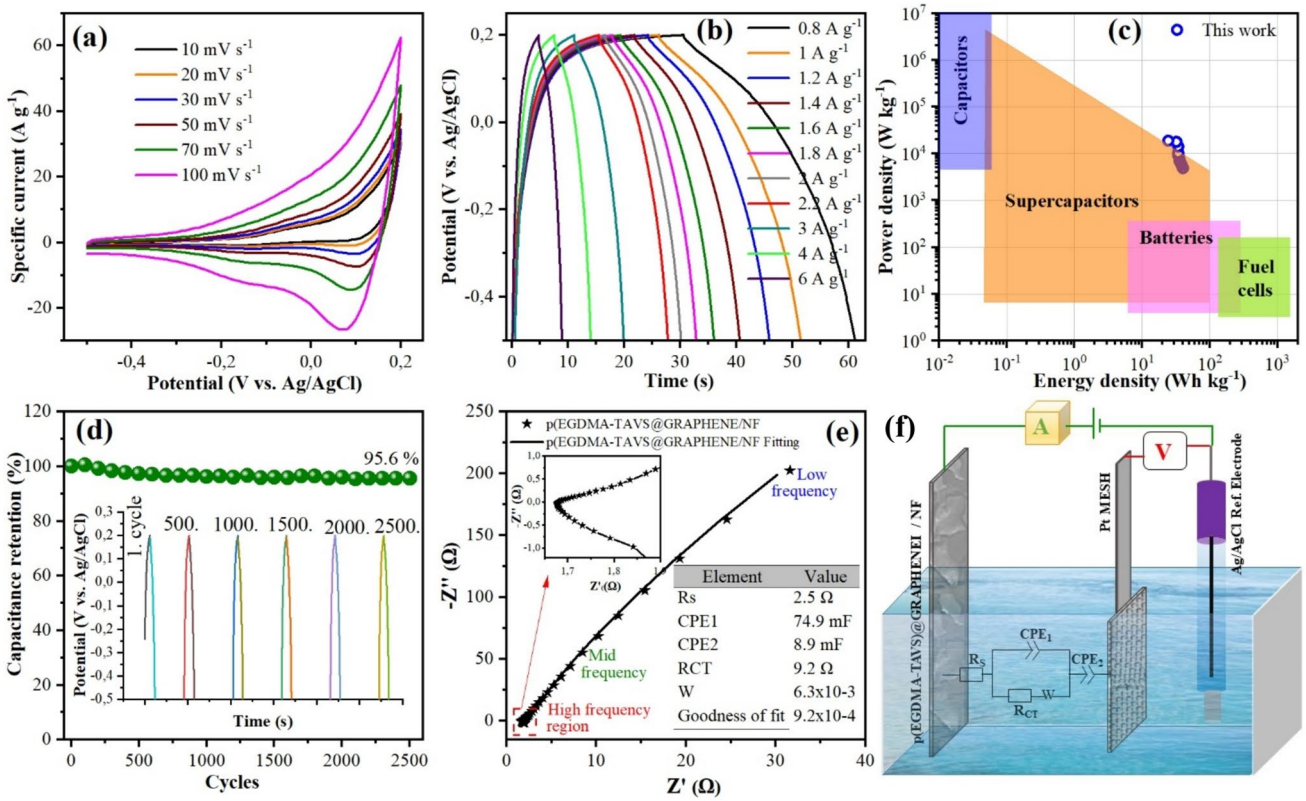


Fig. 6 For p(EGDMA-TAVS)–graphene/NF **a** CV curves depending on scan rate, **b** GCD curves varying with specific current, **c** Ragone plot, which gives the results of this study in comparison with various energy storage systems, **d** Stability test for 2500 cycles (the inset figure displays the GCD variations measured at every 500-cycle interval), **e** Nyquist data with equivalent circuit fitting, and **f** representative illustration of the 3-electrode configuration and equivalent electronic circuit model used in this study

Table 1 Electrochemical performance data from CV and GCD measurements

From CV measurements		From GCD measurements			
Scan rate (mV s^{-1})	C_m (F g^{-1})	Specific current (A g^{-1})	C_s (F g^{-1})	Specific energy (Wh kg^{-1})	Specific power (W kg^{-1})
10	963.9	0.8	592.3	40.3	4773.7
20	817.2	1.0	565.7	38.5	5497.8
30	746.1	1.2	550.0	37.4	6244.7
50	716.4	1.4	530.3	36.1	6910.6
70	650.6	1.6	524.4	35.7	7716.5
100	603.5	1.8	515.8	35.1	8469.2
		2.0	509.4	34.6	9196.8
		2.2	504.7	34.3	10,035.7
		3.0	503.3	34.2	13,822.9
		4.0	475.1	32.3	17,798.2
		6.0	362.5	24.7	21,193.3

efficient electrochemical activity and suggesting that the electrode exhibits a fast charge transfer capability. This behavior reflects the presence of rapid and reversible redox reactions occurring at the electrode/electrolyte interface. A distinct cathodic peak associated with electrode reduction is observed around 0.08 V. Interestingly, this cathodic peak gradually shifts toward more positive potentials as the scan rate increases, which may be attributed to the increased polarization and ion diffusion limitations at higher scan rates.

The specific capacitance of the electrode is determined from the CV measurements according to Eq. (1) [13]:

$$C_m = \frac{1}{mv\left(V_b - V_a\right)} \int_{V_a}^{V_b} idV \tag{1}$$

where C_m (F g^{-1}) shows specific capacitance and I (A g^{-1}) refers to the current intensity. m (g) represents the mass of active material on the Ni foam. $V_b - V_a$ (V) symbolizes the potential window (0.7 V) and v indicates the scanning speed (V s^{-1}). The p(EGDMA-TAVS)–graphene/NF electrode shows specific capacitances decreasing from 963.9 to 603.5 F g^{-1} as the scan rate increases from 10 to 70 mV s^{-1}. Figure 6b displays the galvanostatic charge–discharge (GCD) curves of the electrode at various current densities changing from 0.8 to 6 A g^{-1}. The non-linear GCD curves in Fig. 6b indicate that the electrochemical process is controlled by Faradaic redox reactions. The specific capacitance of the electrode is determined from the GCD curves using Eq. (2) [13]:

$$C_s = \frac{I}{m\Delta V^2} \int Vdt. \tag{2}$$

where C_s (F g^{-1}) represents the specific capacitance, I (A) is the current density, $\int Vdt$ is the area under the discharge curve, t(s) is the discharge time, m(g) is the active material mass on Ni foam, and ΔV(V) expresses the potential window of the electrode (0.7 V). The energy and power densities of the electrode are calculated by using the following relations [14]:

$$E = \frac{C_s \Delta V^2}{2x3.6}. \tag{3}$$

$$P = \frac{3600xE}{\Delta t}. \tag{4}$$

Here, C_s represents the specific capacitance value of the electrode, ΔV is the potential window, and Δt is the discharge duration. The GCD analysis shows that the p(EGDMA-TAVS)–graphene/NF electrode exhibits specific capacitance values of 592.3, 565.5, 550.0, 530.3, 524.4, 515.8, 509.4, 504.7, 503.3, 475.1, and 362.5 F g^{-1} at specific current densities of 0.8, 1.0, 1.2, 1.4, 1.6, 1.8, 2.0, 2.2, 3.0, 4.0, and 6.0 A g^{-1}, respectively (Table 1). The specific energy values at these current densities are 40.3, 38.5, 37.4, 36.1, 35.7, 35.1, 34.6, 34.3, 34.2, 32.3, and 24.7 Wh kg^{-1}, respectively, and the corresponding specific power values are 4773.7, 5497.8, 6244.7, 6910.6, 7716.5, 8469.2, 9196.8, 10,035.7, 13,822.9, 17,798.2, and 21,193.3 W kg^{-1}, respectively (Table 1). It is observed that the electrode possesses greater power density than batteries and fuel cells but has a lower

energy density than fuel cells (Fig. 6c). Figure 6d demonstrates the cycling retention performance of the electrode. After 2500 charge–discharge cycles at 6 A g^{-1}, the electrode retained 95.6% of its initial capacitance, demonstrating excellent cycling stability. The inset graph in Fig. 6d presents the GCD curves recorded at 500-cycle intervals, showing minimal change in shape and duration throughout the test. These results confirm that the p(EGDMA-TAVS)–graphene/NF electrode maintains robust electrochemical performance over extended cycling. The available literature results based on carbon-based materials combined with various polymers and metal oxides, along with the results obtained in this study, are listed in Table 2 [15–26]. The comparison indicates that the performance achieved in this work is competitive and demonstrates the effectiveness of the developed electrodes (Table 2).

Figure 6e shows the Nyquist graph of the electrode. In the Nyquist graph, the linear part observed in the lower frequency region indicates the presence of a diffusion-controlled process and Warburg impedance. The inset graph in Fig. 6e highlights the high-frequency region of the Nyquist plot. Figure 6f shows the equivalent electronic circuit model and the three-electrode cell setup used in the study. In the inset table in Fig. 6e, R_S refers to the solution resistance. The R_S value is 2.5 Ω. R_{CT}, the charge transfer resistance, expresses the speed of the redox reactions occurring between electrolyte and electrode. The R_{CT} value is 9.2 Ω. *CPE* describes the capacitance of the electrical double layer in the interface between electrode and electrolytes. CPE_1 describes the non-ideal capacitive behavior that develops at the electrode/electrolyte boundary, where surface roughness, heterogeneous active sites, and localized charge accumulation prevent the formation of an ideal capacitor. CPE_2 reflects a second capacitive response originating from deeper regions of the electrode structure, where ion diffusion through the porous network and the distribution of reactive sites create an additional phase shift. The CPE_1 and CPE_2 values are, respectively, 74.9 and 8.9 mF. *W* indicates the Warburg impedance. The *W* value is $6.3{\cdot}10^{-3}$ $\Omega s^{-1/2}$. Goodness of fit shows the consistency of the compliance of the equivalent electronic circuit model. The goodness of fit is $9.2{\cdot}10^{-4}$, showing that the

Table 2 Previous studies concerning the energy storage characteristics of carbon-based electrodes

Material	Specific capacitance (F g^{-1})	Energy density (Wh kg^{-1})	Power density (W kg^{-1})	Cycle life	References
rGO/PANI	1348	20	1198	91%@5000	[15]
PANI/CdO/GO	647	116.6	388	82%@500	[16]
rGO-PTs /GCE	1412	8.94	4320	106%@10,000	[17]
PANI/GO	665	365	2684	92%@100	[18]
PANI/GO/h-BN	946	624	2894	98%@100	
PANI/GO/MoS_2	815	260	2356	93%@100	
PANI/GO/TiO_2	713	512	2446	94%@100	
$POP_{TAB\text{-}TPDA}$-rGO	232.4	38.7	1619	81%@7000	[19]
PANI/NiO/Graphene(PNG)	152	59.41	850	89%@2000	[20]
V_2O_5/rGO/PANi hydrogel	982	74.58	2000	94%@10,000	[21]
PAni@OS–rGO	582.6	26.82	882	90%@3000	[22]
PEDOT:PSS/ graphene/$LiTaO_3$	10.14	5.63	16.3	-	[23]
CoNi-C/rGO-2	1177	31.6	750	84%@8000	[24]
Ag NPs/PAC/rGO	527	46	1500	81%10,000	[25]
PAN	40				[26]
0.5NR-10Ni-PAN	25				
1NR-10Ni-PAN	84				
2NR-10Ni-PAN	61				
p(EGDMA-TAVS)–Graphene	592.3	40.3	4773.7	95.6%@2500	This work

CdO cadmium oxide, *PTs* polythiophene, GCE glassy carbon electrode, *h-BN* hexagonal boron nitride, *POP* porous organic polymers, *TAB* 1,3,5-triaminobenzene, *TPDA* 2,5-thiophenedialdehyde, *PNG* PANI/NiO/grapheme, *OS* olive stones, *PSS* polystyrene sulfonate, *CoNi–C* CoNi carbide, *Ag NPs* silver nanoparticles, *PAC* poly(azure C), *PAN* polyacrylonitrile, *NR* natural rubber, *Ni* nickel

compliance of the equivalent electronic circuit model is consistent.

4 Conclusions

This study systematically investigates the energy storage and electrochemical properties of the p(EGDMA-TAVS)–graphene/NF electrode. Electrochemical measurements performed in a three-electrode configuration with 3 M KOH reveal the electrode's substantial energy storage performance. XPS, FTIR, and Raman analyses confirm the presence of the expected atomic and molecular bonds. The porous structure of the electrode enhances its electrochemical performance. The specific capacitance values of the p(EGDMA-TAVS)–graphene/NF electrode are 963.9, 817.2, 746.1, 716.4, 650.6, and 603.5 F g^{-1} at scan rates of 10, 20, 30, 50, 70, and 100 mV s^{-1}, respectively. GCD analysis shows that the p(EGDMA-TAVS)–graphene/NF electrode delivers high performance, with specific capacitances decreasing from 592.3 to 362.5 F g^{-1} as current density increases from 0.8 to 6.0 A g^{-1}. The corresponding specific energy drops from 40.3 to 24.7 Wh kg^{-1}, while specific power rises from 4773.7 to 21,193.3 W kg^{-1}. The capacitance retention of the p(EGDMA-TAVS)–graphene/NF electrode is 95.6% after 2500 cycles at 6 A g^{-1}. These results reveal that the p(EGDMA-TAVS)–graphene/NF electrode is a promising material in energy storage applications with its long cycle life, high specific capacitance, excellent energy, and power density.

Acknowledgements

The authors would like to acknowledge the immense support received from the Research Fund of the Bursa Uludağ University, Project number FGA-2024-1745.

Author Contributions

Petek Balcı contributed toward formal analysis, investigation, writing—original draft, and visualization. Seyit Rıza Tokgöz contributed toward formal analysis, investigation, methodology, and writing—original draft. Ali Kara contributed toward formal analysis, investigation, and visualization. Ahmet Peksöz contributed toward writing—review and editing, supervision, conceptualization, project administration, and validation.

Funding

Open access funding provided by the Scientific and Technological Research Council of Türkiye (TÜBİTAK). The authors have not disclosed any funding.

Data availability

Data will be made available on request.

Declarations

Conflict of interest The authors declare that they have no known competing financial interests or personal relationships that could have appeared to influence the work reported in this paper.

Ethical approval This study does not involve any studies with human participants and/or animals.

Informed consent Informed consent was received from all authors.

Open Access This article is licensed under a Creative Commons Attribution 4.0 International License, which permits use, sharing, adaptation, distribution and reproduction in any medium or format, as long as you give appropriate credit to the original author(s) and the source, provide a link to the Creative Commons licence, and indicate if changes were made. The images or other third party material in this article are included in the article's Creative Commons licence, unless indicated otherwise in a credit line to the material. If material is not included in the article's Creative Commons licence and your intended use is not permitted by statutory regulation or exceeds the permitted use, you will need to obtain permission directly from the copyright holder. To view a copy of this licence, visit http://creativecommons.org/licenses/by/4.0/.

References

1. L. Zhang, X. Wang, S. Bi, J. Chen, Y. Li, Y. Huang, Mater. **10**(11), 1295 (2017)
2. J. Chen, Y. Xu, Y. Zhang, D. Pan, X. Li, W. Liu, J. Mater. Chem. **22**(10), 4279 (2012)
3. R. Liu, H. Zhou, Y. Zhang, S. Wang, J. Li, H. Sun, Mater. **11**(10), 2736 (2021)
4. S. Wang, J. Li, Y. Chen, X. Zhang, Y. Liu, P. Gao, New J. Chem. **46**(36), 12184 (2022)
5. J. Shi, H. Zhang, Y. Li, Q. Chen, T. Wang, Z. Xu, J. Mater. Sci. Mater. Electron. **35**(6), 383 (2024)
6. Y.M. Lu, X. Zhang, H. Wang, L. Chen, J. Zhou, M. Gao, Mater. **17**(1), 23 (2023)
7. Y. Xu, Z. Lin, X. Huang, Y. Wang, Y. Huang, X. Duan, Adv. Mater. **25**, 5779 (2013)
8. H. Tan, D. Xiao, R. Navik, M. Goto, Y. Zhao, J. Mater. Sci. Mater. Electron. **31**, 18569 (2020)
9. Y. Zheng, W. Pann, D. Zheng, C. Sun, J. Electrochem. Soc. **163**, D230 (2016)
10. Y.S. Li, A. Ba, M.S. Mahmood, Spectrochim. Acta A Mol. Biomol. Spectrosc. **72**, 605 (2009)
11. B. Das, R. Kundu, S. Chakravarty, Mater. Chem. Phys. **290**, 126597 (2022)
12. M.H. Mahmood, L. Himics, T. Váczi, I. Ringó, R. Holomb, B. Beiler, M. Veres, J. Raman Spectrosc. **52**(10), 1735 (2021)
13. M. Arslan Çarpan, S.R. Tokgöz, S. Düzyer Gebizli, A. Peksöz, J. Mater. Sci. Mater. Electron. **36**(6), 377 (2025)
14. H. Torun, S.R. Tokgöz, M. Arslan Çarpan, M.H. Somay, A. Peksöz, J. Energy Storage **88**, 111462 (2024)
15. D.C. Pawar, D.B. Malavekar, A.C. Lokhande, C.D. Lokhande, J. Energy Storage **79**, 110154 (2024)
16. A.G. Kenesi, M. Ghorbani, M.S. Lashkenari, Int. J. Hydrogen Energy **47**, 38849 (2022)
17. A.K. Tawade, S.N. Tayade, D.P. Dubal, S.S. Mali, C.K. Hong, K.K.K. Sharma, Chem. Eng. J. **492**, 151843 (2024)
18. M.M. Rahman, M.O. Faruk, M.R. Shawon, M.H. Rahman, M.M.R. Khan, I. Alam, O. Okoli, J. Energy Storage. **67**, 107615 (2023)
19. L. Xu, Y. Li, J. Ni, S. Lv, Y. Li, S. Yan, X. Meng, Electrochim. Acta **503**, 144917 (2024)
20. S. Haider, R. Abid, I. Murtaza, A. Shuja, ACS Omega **8**, 46002 (2023)
21. M. Barazandeh, S.H. Kazemi, F. Roohi, D.S. Haydar, I. Odnevall, ACS Omega **10**, 47973 (2025)
22. I. Benchikh, A.O. Ezzat, L. Sabantina, Y. Benmimoun, A. Benyoucef, Polym. **16**, 421 (2024)
23. M. Aleksandrova, I. Pandiev, Crystals **15**, 660 (2025)
24. E. Aboelazma, C.S. Khea, M.F. Shukura, K.F. Chongc, M.S.M. Saheed, M.B.Z. Hegazy, J. Energy Storage. **72**, 108580 (2023)
25. P. Zou, B. Zhang, C. Wu, H. Zhang, Z. Gan, F. Liu, H.L. Zong, S. Yuan, G. Chen, C. Chen, J. Energy Storage **129**, 117342 (2025)
26. S. Chanthee, C. Asavatesanupap, D. Sertphon, T. Nakkhong, N. Subjalearndee, M. Santikunaporn, Eng. Sci. **27**, 975 (2024)

Publisher's Note Springer Nature remains neutral with regard to jurisdictional claims in published maps and institutional affiliations.